



Perspective

Analytical modeling for redox flow battery design



Yunxiang Chen ^a, Zhijie Xu ^{a,*}, Chao Wang ^{a,b}, Jie Bao ^c, Brian Koeppl ^c, Litao Yan ^c, Peiyuan Gao ^a, Wei Wang ^c

^a Physical and Computational Sciences Directorate, Pacific Northwest National Laboratory, Richland, WA, 99354, USA

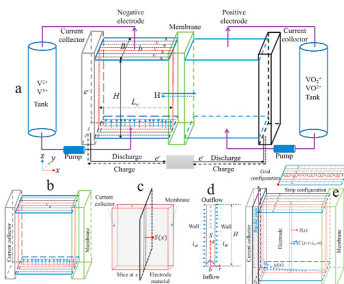
^b Framatome Inc., Richland, WA, 99354, USA

^c Energy and Environment Directorate, Pacific Northwest National Laboratory, Richland, WA, 99354, USA

HIGHLIGHTS

- 2D analytical solutions to over-potential and active species concentrations are presented.
- Formulas for limiting current density and minimum activation over-potential are proposed.
- Effects of operation conditions and electrolyte properties on over-potential are studied.
- A good agreement between the 2D analytical solutions and a finite element model is confirmed.
- Differences between the analytical 2D and a 0D over-potential model are discussed.

GRAPHICAL ABSTRACT



ARTICLE INFO

Keywords:

Redox flow battery
Analytical model
Mass and charge transport
Electrochemical kinetics

ABSTRACT

Deeper market penetration of redox flow batteries requires optimization of the cell performance. Though important for performance optimization, detailed analytical solutions have not been developed for coupled electrolyte flow, mass and charge transport of ions, and reaction kinetics within redox flow batteries. To this end, this work presents analytical solutions to spatial variations of active species concentration and over-potential based on advection-diffusion transport for ions and Butler-Volmer model for interface reaction kinetics. The solutions are validated with results from a finite element model and a calibrated zero-dimensional model. These solutions are then applied to investigate the relationship between over-potential and state of charge, current density, flow velocity, standard reaction rate constant, diffusivity, total active species concentration, and electrode structure. Explicit formulas are identified for minimum activation over-potential and limiting current density as well as their dependence on electrolyte properties, operation conditions, and electrode structure. With our new mathematical formulas, this work provides a theoretical framework for flow battery design.

1. Introduction

The rapid growth of intermittent renewable energies, e.g., wind and

solar power, demands a large number of redox flow batteries (RFBs) due to their long lifecycle, scalability, high efficiency, and site independence [1–4]. However, a massive market penetration of RFBs requires

* Corresponding author.

E-mail address: Zhijie.Xu@pnnl.gov (Z. Xu).

reduction of capital cost to be less than \$150/kWh by 2023 [2,5] from the current cost of \$357–584/kWh [6] of which 42% is contributed by chemical materials [7]. Therefore, for a given redox couple, the most effective approach to reduce costs is to significantly boost the cell performance, which solely depends on addressing critical transport issues and identifying optimized battery design to reduce associated transport losses [3,4]. Among existing RFBs under development, we focus on the transport issues in the all-vanadium redox flow battery (VRFB), which is the most developed and mature technology for commercialization [1,3,8].

The transport of active species, charge, reaction kinetics, and associated transport losses are the key mechanisms determining the overall cell performance [9]; boosting the cell voltage thus necessitates a better understanding of the detailed distribution of associated transport variables, e.g., the concentration of active species, current density, and over-potential. Laboratory-scale experiments have been commonly used to study key mechanisms controlling the overall cell voltage of a VRFB [9–15]; however, they are usually costly and time-consuming, especially for large-scale batteries [1]. Numerical models are playing an increasingly important role in analyzing the detailed transport processes in VRFBs [16]. Specifically at the pore-scale level, detailed distributions of the flow field, over-potential, concentration, state of charge (SoC), and current density around an X-ray scanned realistic electrode have been revealed using a combinatorial lattice Boltzmann method and finite volume method [17]. At the representative-element-volume scale, these distributions have also been demonstrated using three-dimensional (3D) [18–22], two-dimensional (2D) [1,23–27], and one-dimensional (1D) [28,29] simulations by simplifying a realistic electrode as a porous media. Despite the success in modeling small-scale batteries using 3D and 2D numerical models, the long simulation time of these models is a hurdle for their applications in large-scale batteries where a larger number of parameters necessitate optimization [25]. Though 1D and zero-dimensional (0D) models are faster for large-scale problems, their capabilities to handle more realistic situations are challenged, e.g., 1D models cannot account for a non-uniform velocity distribution which is common for serpentine flow channels [30] and 0D models cannot deal with concentration variations along the flow channel which is important at a large current density.

In contrast to the rapid progress in numerical simulations, there is limited progress in the theoretical understanding of the key transport mechanisms, though it is important for reducing the parameter space in experiments, simulations, and optimized battery designs. First, to our best knowledge, existing analytical solutions to the concentration, over-potential, and resulting cell voltage are all based on a 0D assumption and a quasi-steady-state assumption. The quasi-steady-state assumption was rigorously reasoned using a scale analysis together with a plug flow and narrow gap assumption, and validated for typical operation conditions of a VRFB [28]. The 0D models, assuming no variations in concentration along flow channel, are usually reported to reproduce the charge-discharge curve [16,31–33]. However, as these models are only validated against with measured potential at the channel outlet, the assumption of negligible variation in concentration along the flow channel is not reasoned. With this regard, 2D solutions to concentration and over-potential enabling predictions of variations along flow channel are necessary for better flow battery design.

Second, the limiting current density, defined as a current density that makes reactant concentration at the solid electrode interface to be zero, is also an important parameter characterizing cell performance [30]. Though this is intuitive, it is difficult in practice because analytical solutions of reactant concentrations have not been reported. Instead, previous theories quantify the limiting current density by relating it to an effective mass transfer coefficient using Fick's law [8,30,34]. Among these theories, a two-layer (one channel and one porous layer) theory suggests that the effective mass transfer coefficient calculated as the average flow velocity penetrating from the channel to the porous media gives the best estimation of the limiting current density when compared

with measured ones in experiments [30,35]. Though without rigorous demonstration, their theory along with the experiments by Ref. [13] further implies that the effective mass transfer coefficient is affected by the average flow velocity at the entrance of the flow channel. A theoretical model for limiting current density is thus necessary to better understand its dependence on flow, transport properties, and channel geometry.

Therefore, to provide a theoretical framework for reducing parameter space for experiments, simulations, and optimized designs, as well as a better explanation of the limiting current density, this work aims to first derive analytical solutions to concentrations of active species and over-potential, then determine the limiting current density by making reactant concentration to be zero, and finally study how operation conditions (SoC, applied current density, flow velocity, total concentration), electrode and chemical materials (standard reaction rate constant and active ion diffusivity), and electrode structure (channel width and length) affect the distribution of over-potential. Following these purposes, the paper is organized as follows: the governing equations for reactant concentrations and ionic potential, associated assumptions, and boundary conditions are introduced in Section 2, followed by the derivation of the analytical solutions using a reduced boundary method in Section 3. The resulting analytical solutions were then verified with results from a finite element model and compared with a 0D model in Section 4. Two new formulas for limiting current density and the effects of operation conditions, electrode and chemical properties, and channel size on over-potential distribution are proposed and discussed in Section 5 and Supplementary Information S1 – S4.

2. Physical and mathematical models

2.1. Model assumptions and equations

Fig. 1a shows the components of a RFB, including two reservoir tanks for electrolyte storage and supply, two pumps, two current collectors, two electrodes, and one membrane. The electrode is simplified as either a strip configuration or a grid configuration (**Fig. 1e**) to make the following mathematical derivations tractable but retain a similarity to the actual pore structure in the electrode. The simplified electrode is composed of many microchannels separated by solid electrode materials which are denoted by c and s respectively in **Fig. 1a**, b, and e. L_e , H , and B in **Fig. 1a** denote the length, height, and width of the negative half cell. b is the width of an individual microchannel, which can be estimated by $b = 2\epsilon/A_s$ for strip configuration or $b = 4\epsilon/A_s$ for grid configuration with ϵ and A_s denoting electrode porosity and specific area, respectively (see derivations in [Appendix A.1](#)). x , y , and z denote spatial coordinates.

Key transport processes occurring during battery operation include a recursive transport of electrolyte flow between the reservoir tank and the microchannels (marker c in **Fig. 1a**) in the electrode, transport of charged ions in the flow channels, and chemical reactions at the interface between flow channels and solid electrode materials (marker s in **Fig. 1a**). For cells with flow-by channels, the electrolyte is recirculated between the bipolar plate and the tank, and a portion of the electrolyte moves into the microchannels in the electrode from the flow channels in the bipolar plate. The electrolyte velocity in this scenario is not uniform but varies along cell thickness direction x (blue arrows in **Fig. 1e**). An analytical solution to the velocity can be found in Ref. [30]. During discharge, in the positive electrode, VO_2^+ converts to VO^{2+} through the electrochemical reaction $\text{VO}_2^+ + 2\text{H}^+ + \text{e}^- \rightarrow \text{VO}^{2+} + \text{H}_2\text{O}$, while in the negative electrode, V^{2+} converts to V^{3+} through the electrochemical reaction $\text{V}^{2+} \rightarrow \text{V}^{3+} + \text{e}^-$. The reactions are reversed during charge. Because the reactions in positive and negative electrodes share very similar mechanisms, we focus on the negative electrode to demonstrate the proposed analytical solution.

To obtain an analytical solution to the key transport processes, we focus on one individual channel in the negative half cell during discharge as shown in **Fig. 1b**. The actual sizes of an individual channel,

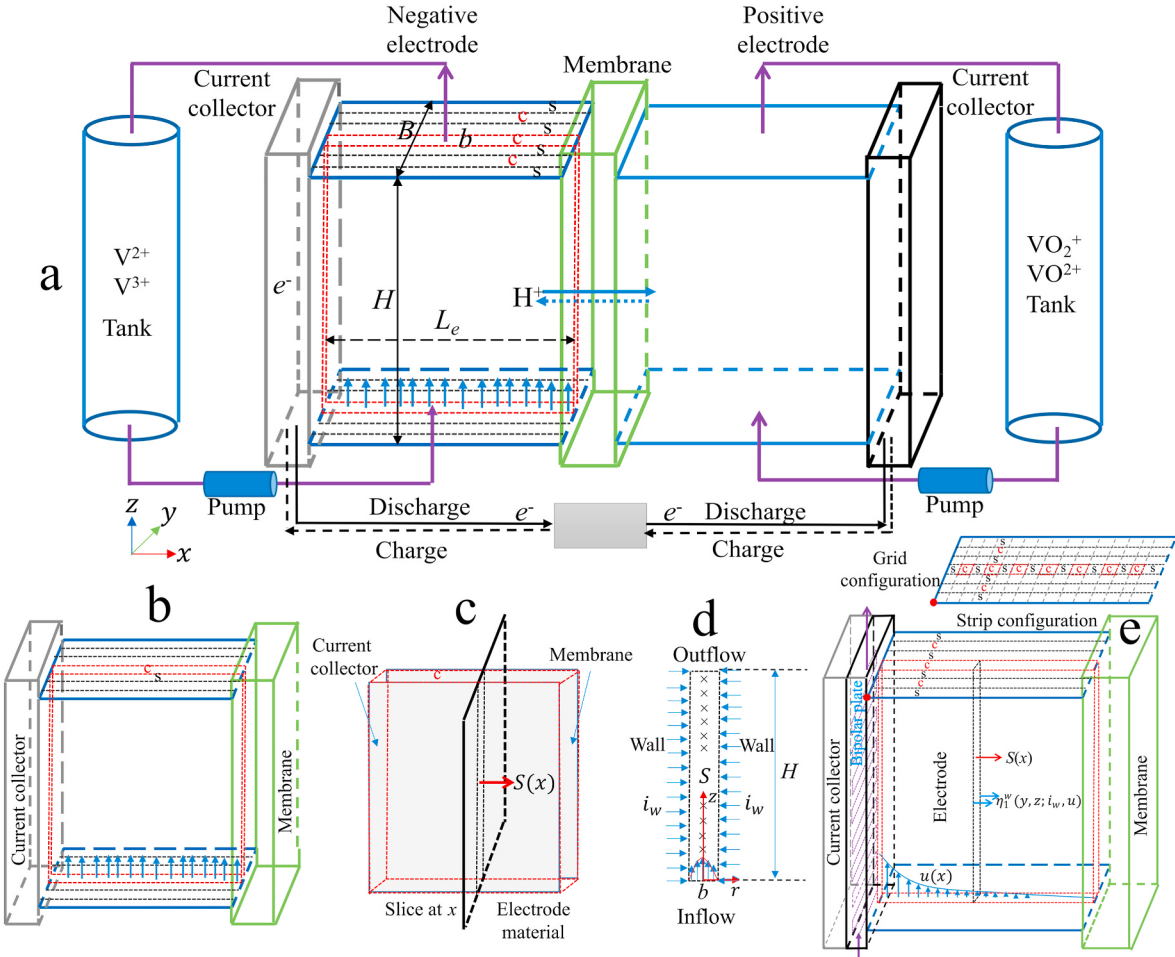


Fig. 1. A sketch of a VRFB (a), a simplification from the 3D half cell (b) to a 2D slice (c,d), and a sketch of a cell with a bipolar plate, a flow channel, and strip and grid configuration (e). Markers c and s denote channels and electrode solids. $S(x)$ denotes an ionic flux gradient source passing through a slice at cross-section x , and H , b , i_w , u , and η_l^w denote the height, width, local wall current density, streamwise flow velocity, and wall over-potential, respectively. Red dots in (e) denote the potential measurement point in experiments by Pacific Northwest National Lab (PNNL). Figures not to scale. (For interpretation of the references to colour in this figure legend, the reader is referred to the Web version of this article.)

including height, length, and width, usually satisfy $H \gg L_e \gg b$. For example, a realistic RFB cell has a width and length as $H = 100$ mm and $L_e = 4$ mm [1], and b has a value ranging from $10\ \mu\text{m}$ to $600\ \mu\text{m}$ [3,17, 36]. Besides, it was reported that variations of active species concentration and current density along cell thickness direction (x -direction) are less than 10% of their average values over the x -direction [17,37, 38]. These conditions mean that the variations in concentration and current density at a cross-section x and its infinite-close neighbor $x + dx$ are negligible, and therefore a 2D slice can be used to capture the main behaviors of the transport processes in an infinitesimal volume between x and $x + dx$ as shown in Fig. 1c. For any slice at x , the effects of variations in local current density and flow velocity on the transport processes can also be evaluated by introducing a distributed velocity and current density such as $u(x)$ and $i_w(x)$. Following such a concept, we cut a slice at coordinate x (Fig. 1c) and study the flow, concentration, charge, and chemical reactions on such a 2D slice (Fig. 1d). The effects of flow channel design and electrode pore structure design can also be evaluated by introducing a distributed velocity and current density as shown in Fig. 1e. It is worth mentioning that the square channels in the negative half cell could also be circular in real electrodes; therefore, we use a cylindrical coordinate r to represent both situations instead of using a Cartesian coordinate y .

The flow in the channels is usually laminar. Under the assumption of a fully developed flow, the flow velocity in the 2D sliced channel is $\vec{U} =$

$(0, 0, u)$ with $u = u_m[1 - (2r/b)^2]$ [39] where u_m is the centerline velocity. Define $d = 0$ (square) and $d = 1$ (circular) to represent the effect of channel shape, then the centerline velocity can be determined by $u_m = u_0(3+d)/2$ with u_0 denoting the cross-sectional average velocity. For the flow-through electrode as shown in Fig. 1a, the velocity can be estimated from the volumetric pump rate (ω) by $u_0 = \omega/(BL_e\epsilon)$ for strip and grid configuration (see derivations in Appendix A.1). For an electrode with flow-by channels, inlet velocity u_0 needs to be determined from numerical or analytical models for a given flow field design. For example, an analytical solution to the flow velocity in a serpentine flow channel was reported in Ref. [30].

The transport of reaction species in a RFB is a key process. Considering a VRFB, the transport of V²⁺ and V³⁺ in the negative electrode can be modeled by Equation (1) and Equation (2) [17].

$$\frac{\partial c_2}{\partial t} + \vec{U} \cdot \nabla c_2 = D_2 \nabla^2 c_2 \quad (1)$$

$$\frac{\partial c_3}{\partial t} + \vec{U} \cdot \nabla c_3 = D_3 \nabla^2 c_3 \quad (2)$$

where c_2 and c_3 denote the concentration of V²⁺ and V³⁺, and D_2 and D_3 denote their diffusion coefficients. It is also worth mentioning that the migration term due to the electrokinetic effect has been neglected because of its insignificant effects on the transport of species [24].

The charge transport of ions (quantified by ionic potential ϕ_e) in the electrolyte is another crucial process within a RFB, which can be described by Equation (3).

$$\nabla \cdot (k_{eff} \nabla \phi_e) + \nabla \cdot (F \sum z_j D_j \nabla c_j) = 0 \quad (3)$$

where $k_{eff} = \frac{F^2}{RT} \sum z_j^2 D_j c_j$ with z_j , D_j , and c_j denoting valence, diffusivity, and concentration of the species j. F , R , and T denote Faraday constant, ideal gas constant, and electrolyte temperature, respectively. As the electrolyte is electroneutral, the net charge fluxes of all charged ions are zero, which can be quantified by $\sum z_j c_j = 0$.

To obtain an analytical solution for ϕ_e , we consider the charged ions in the negative electrode with two assumptions: the electrolyte is in a steady state and the diffusivities of V^{2+} and V^{3+} are approximately identical. For the charged non-active ions, i.e., H^+ , HSO_4^- , and SO_4^{2-} , their transports are governed by a similar equation as Equation (1). In a steady state, their solutions are constant if the inlet concentration is uniform and no reaction occurs at the wall (Fig. 1d). With the two assumptions, k_{eff} can be approximately treated as a constant and the second term in Equation (3) becomes zero (see simplifications in Appendix A.2). Considering a 2D slice at location x as a control volume, the charge conservation means $-2Hi_w(x) + bHS(x) = 0$ and thus $S(x) = 2i_w(x)/b$ with $i_w(x)$ denoting a local current density at the interface between a channel and the neighboring electrode material. Note that $S(x)$ is the gradient of the current density of charged ions at an arbitrary cross-section x and it has to be generated from an externally applied current I_t . For convenience, we define a nominal current density I_0 as the average current density applied to the interface between the current collector and the electrode. For a strip configuration, the charge conservation of electrons means $I_t = I_0 BH = 2NH \int_0^{L_e} i_w(x) dx$ with N denoting the number of channels in the electrode. By assuming a uniform wall current density, an average local current density can be estimated by $i_w = I_t/(L_e B H A_s) = I_0/(L_e A_s)$. This formula also holds for the grid configuration (see derivations in Appendix A.1). It is worth mentioning that the effects of the wall current density variation on the transport processes can be directly evaluated if a distribution or value of the wall current density is given. Therefore, with the above two assumptions and conservation of charge, Equation (3) can be reduced to Equation (4). For a narrow gap as shown in Fig. 1d ($H \gg b$), such an equation further shows that the wall current density i_w and $S(x)$ is approximately constant along z -direction, which is validated with results from a 3D pore-scale modeling by Ref. [17]. It is worth mentioning that such a simplification may not hold for large-scale cells, in which situation a z -coordinate dependent wall current density could be used to replace the uniform current density as shown in Equation (24).

$$k_{eff} \nabla^2 \phi_e = S(x) \quad (4)$$

2.2. Boundary conditions

Considering the 2D slice as shown in Fig. 1d, it is clear that we need to specify boundary conditions for concentration at the two walls, inlet, and outlet in order to obtain an analytical solution to Equation (1). The boundary condition for concentration V^{2+} , V^{3+} , and ϕ_e at the walls is determined through the reaction kinetics, i.e., the Butler-Volmer equation, which has the form as Equation (5) [40].

$$\vec{J}_2 \cdot \vec{n} = -\vec{J}_3 \cdot \vec{n} = i_0 [e^{(1-\alpha)f\eta_1^w} - e^{-\alpha f \eta_1^w}] \quad (5)$$

where \vec{J}_2 and \vec{J}_3 denote driving fluxes of V^{2+} and V^{3+} at the walls. Note that convective fluxes are zero and electrokinetic-generated fluxes are negligible at the walls, thus \vec{J}_2 and \vec{J}_3 only represent diffusive fluxes. i_0 is the exchange current at the interface between channels and solid materials and is calculated by $i_0 = k_1 (c_2^w)^{\alpha} (c_3^w)^{1-\alpha}$ with k_1 , α , c_2^w , and c_3^w denoting a standard reaction rate constant, transfer coefficient,

and concentration of V^{2+} and V^{3+} at the walls, respectively. f is a constant defined as $f = F/(RT)$ and η_1^w is the over-potential at the walls defined by $\eta_1^w = \phi_s^w - \phi_e^w - \left[E_1^0 + \frac{1}{f} \ln \left(\frac{c_3^w}{c_2^w} \right) \right]$. Here ϕ_s^w and ϕ_e^w are the electronic potential and ionic potential at the walls, and E_1^0 is the standard potential of V^{2+}/V^{3+} pair.

In experiments, we usually control the current applied to the battery and then measure the resulting potential. To make our analytical modeling more similar to experiments, we apply a total current (I_t) to the interface between the current collector and the electrode and estimate the wall current density as shown in Section 2.1. For convenience, we denote the local wall current density by I , i.e., $I = i_w = I_0/(L_e A_s)$. With such a definition, the boundary condition for V^{2+} at the walls becomes $\vec{J}_2 \cdot \vec{n} = -D_2 \frac{\partial c_2}{\partial z}|_{z=H} = I/F$. At the outlet, the flux of V^{2+} is zero and thus $-D_2 \frac{\partial c_2}{\partial z}|_{z=H} = 0$. As the concentration is identical to the entrance concentration before reaching a fully developed region, we have $c_2|_{z=z_e, r=0} = c_2^i$ where z_e denotes an entrance length and is calculated by $z_e/b = \gamma Pe$. The value γ is constant and has a value of about 0.033 [41]. $Pe = u_0 b / D_2$ denotes a Peclet number.

As Equations (1) and (2) are linear equations and $(\vec{J}_2 + \vec{J}_3) \cdot \vec{n} = 0$, the summation of c_2 and c_3 , i.e., $c_{23} = c_2 + c_3$, should satisfy Equation (1) with a boundary condition $\frac{\partial c_{23}}{\partial z}|_{z=H} = 0$ at the walls. With $\frac{\partial c_{23}}{\partial z}|_{z=b/2} = -I/(FD_2)$ at the outlet and $c_{23}|_{z=0} = c_{23}^i = c_2^i + c_3^i$ at the inlet, the solution of c_{23} is a uniform distribution, i.e., $c_{23} = c_{23}^i$. Therefore, the solution to c_3 can be determined by $c_3 = c_{23}^i - c_2$.

3. Reduced boundary method and analytical solutions

Section 2 showed that only Equation (1) is required to be solved with boundary conditions $c_2|_{z=z_e, r=0} = c_2^i$, $\frac{\partial c_2}{\partial z}|_{z=H} = 0$, and $\frac{\partial c_2}{\partial z}|_{z=b/2} = -I/(FD_2)$. In this work, the reduced boundary method [42] was used to derive an analytical solution to the concentration of V^{2+} at the centerline and the wall, i.e., $c_2^{*} = c_2^i/c_{23}^0$ and $c_2^{w*} = c_2^w/c_{23}^0$, as shown in Equations (6) and (7). Accordingly, the solution to V^{3+} at the centerline and the wall is $c_3^{*} = c_3^i/c_{23}^0 = 1 - c_2^{*}$ and $c_3^{w*} = c_3^w/c_{23}^0 = 1 - c_2^{w*}$ (see Appendix A.3 for details of the reduced boundary method and derivations).

$$c_2^{*} = SoC - \frac{6(d+1)}{d+3} I_{cu} \left(\frac{z}{b} - \gamma Pe \right) - \frac{12(d+1)}{(d+3)^2} \frac{I_{cu}}{Pe} \left[e^{\frac{d+3}{2} Pe \left(\gamma Pe - \frac{H}{b} \right)} - e^{\frac{d+3}{2} Pe \frac{z-H}{b}} \right] \quad (6)$$

$$c_2^{w*} = SoC - \left[\frac{5}{16} - \frac{6(d+1)}{d+3} \gamma \right] I_{cd} - \frac{6(d+1)}{d+3} \frac{I_{ct}}{b} z - \frac{12(d+1)}{(d+3)^2} \frac{I_{cu}}{Pe} \left[e^{\frac{d+3}{2} Pe \left(\gamma Pe - \frac{H}{b} \right)} - e^{\frac{d+3}{2} Pe \frac{z-H}{b}} \right] \quad (7)$$

With solutions of c_2^{*} and c_2^{w*} , over-potential at the walls can be obtained by solving the Butler-Volmer equation as shown in Equation (8).

$$\eta_1^w = \frac{RT}{aF} \ln \left(\frac{I_{ck}}{2\sqrt{c_2^{w*}(1-c_2^{w*})}} + \sqrt{\frac{I_{ck}^2}{4c_2^{w*}(1-c_2^{w*})} + 1} \right) \quad (8)$$

where non-dimensional parameters in c_2^* , c_2^{w*} and η_1^w are defined as: $SoC = \frac{c_2^i}{c_{23}^0}$, $I_{cd} = \frac{I}{F c_{23}^0 D_2 / b^3}$, $I_{cu} = \frac{I}{F c_{23}^0 u_0}$, $Pe = \frac{u_0 b}{D_2}$, and $I_{ck} = \frac{I}{F c_{23}^0 k_1}$. Here I_{cd} , I_{cu} , and I_{ck} are used to quantify the relative importance of local driving current density to the characteristic current density generated from mass and charge transfer due to diffusion, advection, and chemical reaction, respectively. Section 5 further links I_{cu} and I_{ck} to the reaction stoichiometric availability and the charge-transfer resistance, respectively.

4. Comparison with finite element model and 0D model

4.1. Verification with a finite element model

To verify the analytical solutions as Equation 6 through 8, we developed a 2D finite element numerical model in COMSOL (www.comsol.com) and compared its solutions with those from the analytical solutions. The Comsol model numerically solves Equation (1) with the boundary conditions discussed in Section 2.2 for a 2D microchannel. The control parameters for concentration and over-potential include local current density I , microchannel width b , diffusivity D_2 , total concentration c_{23}^0 , and mean flow velocity u_0 . Therefore, we compared Comsol data with our analytical solutions for one base case (Fig. 2a and Table 1 column 3) and five extra cases with different control parameters as shown in Fig. 2b-f. The result suggests that the analytical solutions for centerline concentration (c_2^* , blue dashed lines), wall concentration (c_2^{w*} , black dashed lines), and wall over-potential (η_1^w , red dashed lines) agree well with results (blue circle, black cross, and red diamond) from Comsol after a short distance (vertical dashed lines) away from the entrance. Such a distance is termed a concentration entrance length (z_e) and is calculated as a distance where the centerline concentration (blue circle) is about 0.5% lower than that at the entrance. With the Comsol data, we show that the concentration entrance length is similar to a thermal entrance length, which can be calculated by $z_e/b = \gamma Pe$ with $\gamma \approx$

0.033 [41]. It is worth mentioning that a quantitative definition of an entrance length for a wall concentration is difficult because chemical reaction affects wall concentration immediately after the entrance; however, its location (intersection locations between black dashed lines and black cross lines) is close to the entrance length defined by centerline concentration. For the validation cases shown here, z_e is about 14 ~ 41 times of the microchannel width, b , or 14% ~ 41% of the channel height, H . For real applications, an electrode cell can be represented by multiple small channels, i.e., large channel number N , therefore the entrance length is likely much smaller than the channel height. For instance, the ratio of the cell height to an estimated microchannel size is 936.5 for an actual electrode used in PNNL experiments (see Fig. 3b and parameters in Table 1 column 4), which means our analytical solutions are applicable to most of the regions in an electrode. The comparison also shows that the wall concentration deviates from the centerline concentration by $\frac{5}{16}I_{cd}$, which suggests a new approach to link the bulk concentration to the interface concentration for 2D models rather than using a linear dependence assumption [1].

4.2. Comparison with experimental data and zero-dimensional model

As predicting the cell voltage is a primary goal for flow battery modeling and the over-potential is an important quantity but difficult to measure, we use the following procedure to illustrate the difference in over-potential from our model as compared to experimental data and 0D

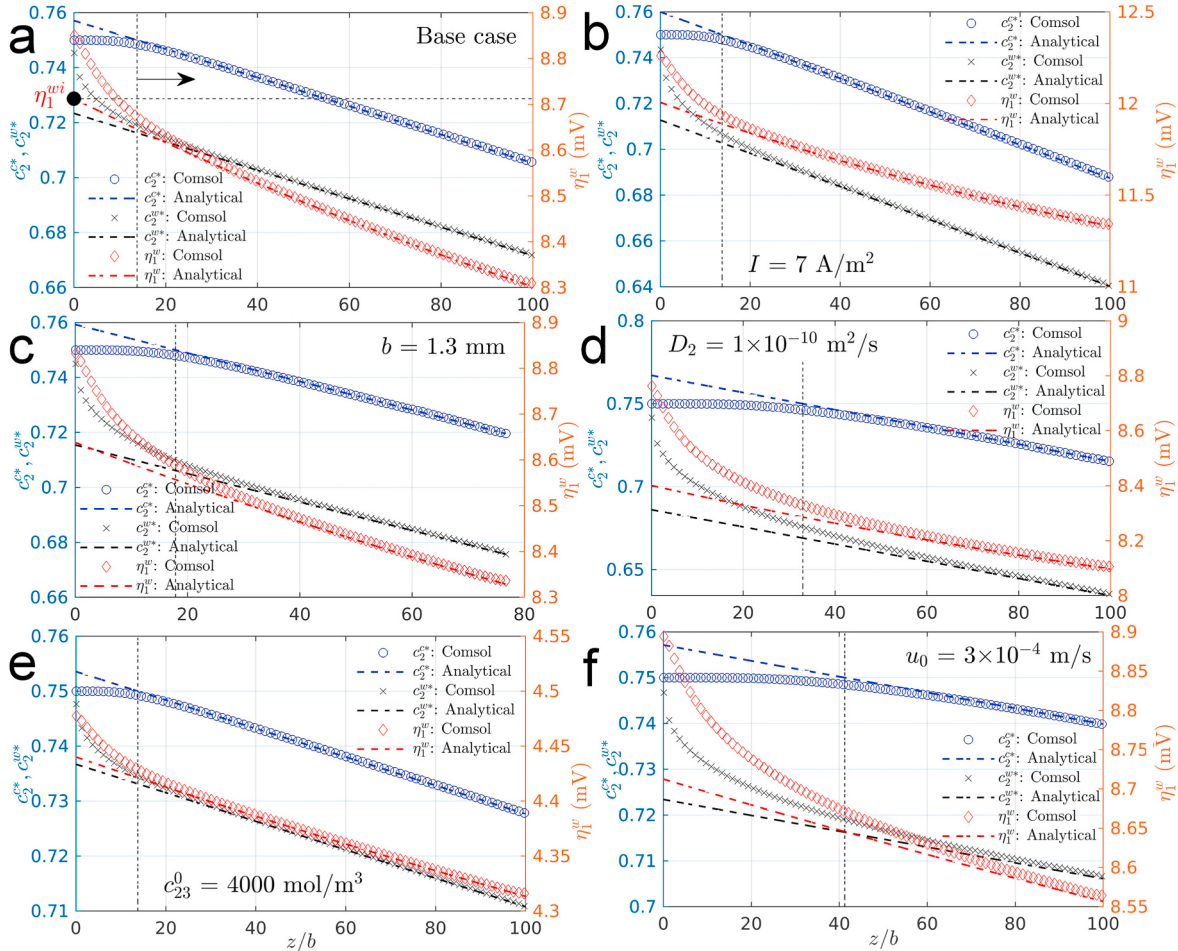


Fig. 2. A comparison of analytical solutions to centerline concentration (c_2^* , blue dashed lines), wall concentration (c_2^{w*} , black dashed lines), and wall over-potential (η_1^w , red dashed lines) with results from Comsol. (a) is a base case using parameters listed in Table 1(column 3) and (b-f) denote cases with one parameter different from the base case as shown in each figure. Vertical dashed lines in (a-f) indicate locations of the concentration entrance length. The horizontal arrow in (a) denotes regions where analytical solutions are applicable. (For interpretation of the references to colour in this figure legend, the reader is referred to the Web version of this article.)

Table 1

Parameters used for Comsol base case and 0D model comparison.

Symbol	Meaning	Comsol Base case	0D Model					Unit
			0D - b	0D - c	0D - d	0D - e	0D - f	
SoC	state of charge	0.75	0.75 ~ 0*	0.75 ~ 0	0.75 ~ 0	0.75 ~ 0	0.75 ~ 0	1
H	cell height	0.1	0.05*	0.05	0.05	0.05	0.05	m
I	local wall current density	5	7.18*	7.18	7.18	7.18	7.18	A/m ²
b	microchannel width	1000	53.4*	53.4	53.4	53.4	53.4	μm
D_2	diffusivity of vanadium V ²⁺	2.4e-10	2.4e-10*	2.4e-9	2.4e-10	2.4e-9	2.4e-10	m ² /s
c_{23}^0	total concentration of V ²⁺ /V ³⁺	2000	1500*	1500	1500	1500	1500	mol/m ³
ω	pump rate	—	20*	20	200	200	2	ml/min
u_0	average flow velocity	0.1	6	6	60	60	0.6	mm/s
k_1	standard rate constant	1.7e-7	1.7e-7*	1.7e-7	1.7e-7	1.7e-7	1.7e-7	m/s
I_{cd}	$\frac{I}{F c_{23}^0 D_2 / b}$	0.108	1.1e-2	1.1e-3	1.1e-2	1.1e-3	1.1e-2	1
I_{cu}	$\frac{F c_{23}^0 u_0}{I}$	2.6e-4	8.3e-6	8.3e-6	8.3e-7	8.3e-7	8.3e-5	1
I_{ck}	$\frac{F c_{23}^0 k_1}{u_0 b}$	0.15	0.292	0.292	0.292	0.292	0.292	1
Pe	$\frac{F c_{23}^0 k_1}{u_0 b}$	416.7	1.33e3	1.33e2	1.33e4	1.33e3	1.33e2	1

Data with * denote parameters used in Pacific Northwest National Laboratory experiments. Other experimental parameters include: cell width $B = 2$ cm, cell thickness $L_e = 3$ mm, electrode porosity $\varepsilon = 0.929$, specific area $A_s = 3.48e4$ m²/m³, total current $I_t = 0.75$ A. The microchannel width b is estimated using the strip configuration.

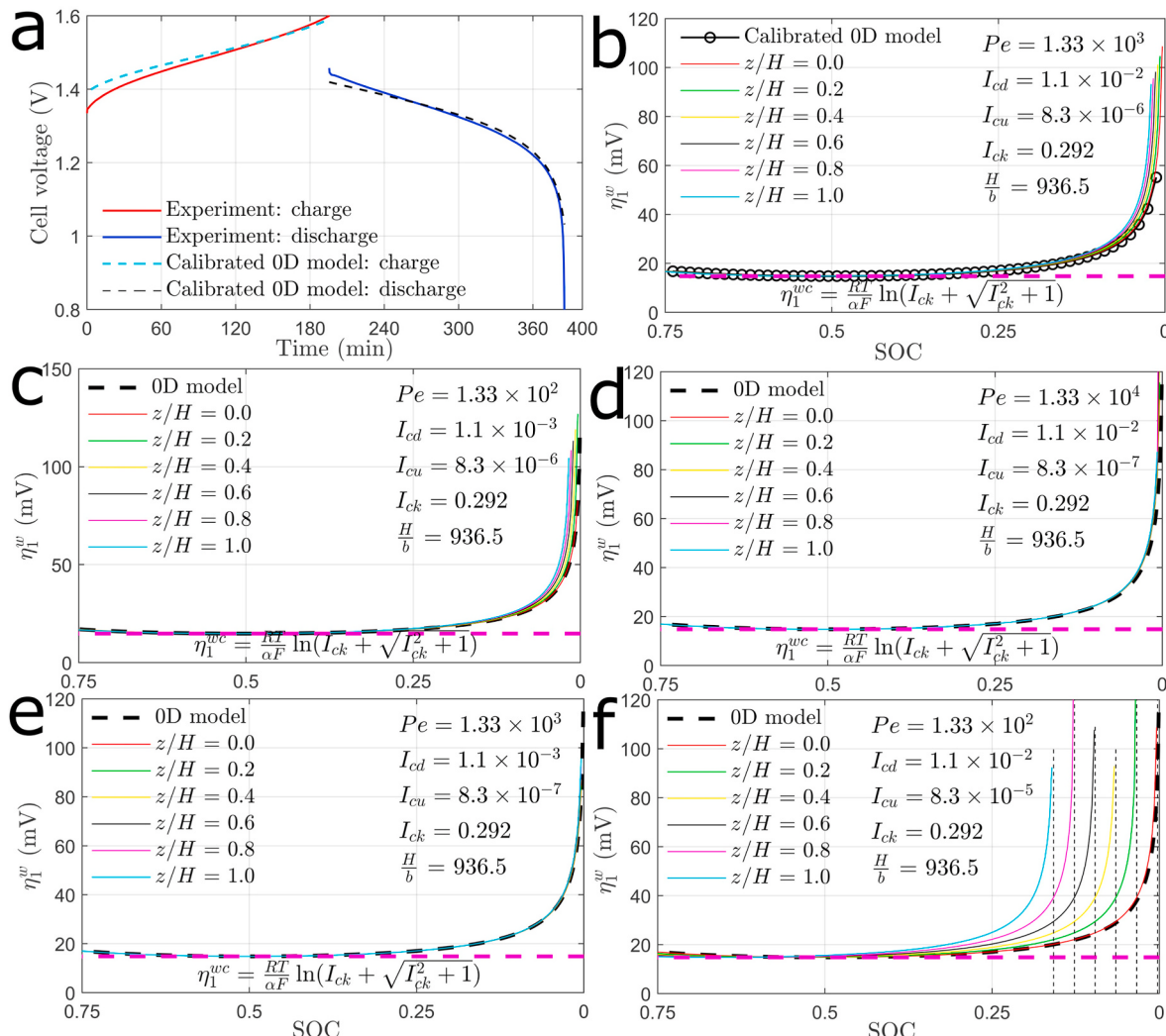


Fig. 3. A comparison of cell voltage from experiment and a 0D cell voltage model from Ref. [33] (a); and the comparison of the over-potential from the calibrated 0D model with those from the new analytical solution under different non-dimensional parameters (b-f). Parameters used in (a-f) are listed in Table 1.

model. Firstly, we calibrate the standard reaction rate constant required in a commonly used 0D cell voltage model [33] using the measured cell voltage (at the location marked by the red dot in Fig. 1e) during a charge-discharge cycle; then the over-potential calibrated in the 0D cell voltage model is used as a reference over-potential in our analytical model. Fig. 3a shows that using the calibrated standard reaction rate constant can well reproduce the cell voltage observed in the experiment. Using identical calibrated reaction rate constant k_1 and other parameters in the experiments, Fig. 3b shows over-potential calculated from the calibrated 0D model and those from our new analytical solution. It shows that the over-potential at the entrance ($z/H = 0$) from our model overlaps with that from the calibrated 0D model. However, a larger difference is observed at locations away from the entrance (lines with $z/H > 0$). These results suggest that our analytical solution can at least accurately predict the over-potential at the entrance, which is important for good prediction of the cell voltage. With the available solutions to active species concentration and over-potential, a new analytical cell voltage model can be established by substituting these solutions into the equations of open circuit potential and activation losses as those used in the 0D cell voltage model [33].

To further illustrate the differences between our model and the widely used 0D model, i.e., Equation (10), Fig. 3c-f compares the over-potential from our model and the 0D model at different locations and parameters. The result shows that a better agreement between our analytical model and the 0D model can be achieved with a higher diffusivity (lower I_{cd} in Fig. 3c) or a higher flow velocity (lower I_{cu} in Fig. 3d). It is observed that over-potentials at all locations from our model overlap with those predicted from the 0D model when diffusivity and flow velocity both increase 10 times (Fig. 3e). This happens because a sufficient fast advection (high flow velocity) and diffusion (high diffusivity) of the reactants reduces the concentration difference in the bulk flow and at the electrode interface. Such a situation satisfies the assumption of a 0D model. On the other side, this also suggests that the 0D model may not be reliable for a flow battery where non-uniformity of active species concentration is important, e.g., at a low velocity scenario (higher I_{cu}) as shown in Fig. 3f. Increasing the flow velocity reduces the mass transport resistance, however, it also increases the energy consumed by pump and thus may result in a lower system efficiency. Therefore, flow velocity optimization is necessary for minimizing both over-potential and pump energy consumption. Despite the differences between our model and the 0D model, it is worth mentioning that both 0D model and our analytical model can predict a minimum over-potential as Equation (9) (pink dashed lines in Fig. 3) which is solely determined by the non-dimensional number I_{ck} . This suggests the necessity to develop new electrode materials with a higher standard reaction rate constant because improvements in flow velocity, diffusion, and channel size cannot reduce the minimum over-potential. Note that the 0D model assumes no concentration gradient in the channel, therefore, the minimum over-potential is actually a minimum activation over-potential.

$$\eta_1^{wc} = \frac{RT}{\alpha F} \ln \left(I_{ck} + \sqrt{I_{ck}^2 + 1} \right) \quad (9)$$

Our model also shows that the minimum SoC a battery can achieve during discharge varies along the channel. Such a SoC can be quantified by $\left(\frac{5}{16} - 2\gamma\right)I_{cd} + 2I_{cu}\frac{H}{b}\frac{z}{H}$ (vertical dashed lines in Fig. 3f) through setting $c_2^{w*} = 0$, $d = 0$, and neglecting the last term in c_2^{w*} . Further, Fig. 3 shows different behaviors in over-potential at initial discharge (SoC = 0.75) and the end of discharge (SoC at maximum over-potential) and how current density, advection, diffusion, and initial concentration affect such a difference, e.g., lower flow velocity and lower diffusivity result into high I_{cu} and I_{cd} and thus shift the lowest SoC to higher values.

$$\eta_1^{w0} = \frac{RT}{\alpha F} \ln \left(\frac{I_{ck}}{2\sqrt{\text{SoC}(1-\text{SoC})}} + \sqrt{\frac{I_{ck}^2}{4\text{SoC}(1-\text{SoC})} + 1} \right) \quad (10)$$

5. Results and discussion

5.1. Limiting current density

As the concentration at the centerline and wall decreases along flow direction during discharge and the concentration at the wall decreases faster than that at the centerline, we define a local limiting current density as the current density that makes $c_2^{w*} = 0$ at the outlet. Following Equation (7) and considering a rectangular channel ($d = 0$), the local limiting current density is estimated by Equation (11). Similar to the relationship between a local current density and the nominal current density, a nominal limiting current density can be calculated by $I_{c0} = I_c L_e A_s$, which is a more commonly used term in an actual flow battery.

$$I_c = \frac{Fu_0 c_{23}^0 \text{SoC}}{(5/16 - 2\gamma)Pe + 2H/b - 4/(3Pe)} \quad (11)$$

Equation (11) means that the limiting local current density increases linearly with SoC and total concentration, which agrees with existing theories. In general, previous theories on limiting current density can be written as $I_c = k_m^* F c_{23}^0 \text{SoC}$ with k_m^* denoting a lumped mass transfer coefficient. Three formulas of k_m^* were reported based on different control mechanisms of current density, e.g., $k_m^* = A_s b_s k_m$ based on diffusion boundary layer [8,43], $k_m^* = 0.9783 \frac{D_2}{H} \int_0^H \left(\frac{u_f}{b D_2 z} \right)^{1/3} dz$ by assuming no electrolyte penetration between two parallel plates [34], and $k_m^* = \frac{Q_p}{H L_e}$ based on a two-layer electrode assumption [30]. The existence of different formulas suggests that the limiting current density is controlled by multiple factors, including the specific surface area (A_s), fiber size (b_s), diffusivity (D_2), height of flow channel (H), microchannel width (b), distribution of electrolyte velocity in porous media (u_f), flow rate penetrating from electrolyte to electrode (Q_p), and channel length (L_e). In our model, the lumped mass transfer coefficient is $k_m^* = \frac{u_0}{(5/16 - 2\gamma)Pe + 2H/b - 4/(3Pe)}$, which reflects the effects of inflow velocity (flow rate), entrance effect, diffusion, cell height, and microchannel size. As the microchannel size $b = 2e/A_s$ or $b = 4e/A_s$, our formula for k_m^* reflects the effects of porosity and specific surface area on the limiting current density.

As the mass transfer is usually controlled by the mass transport polarization between the bulk concentration (c_b) and interface concentration (c_0), which can be quantified by Fick's law as $I = FD_2 \frac{c_b - c_0}{\delta_d}$, the limiting current density can also be determined by $I_c = FD_2 \frac{c_b}{\delta_d} \approx F c_{23}^0 \text{SoC} \frac{D_2}{\delta_d}$ when the interface concentration c_0 becomes 0 [37]. Therefore, quantifying the mass transfer coefficient is equivalent to estimate the diffusion layer thickness δ_d . From this viewpoint, the diffusion layer thickness can be quantified by $\delta_d = \beta D_2 / u_0$ with $\beta = (5/16 - 2\gamma)Pe + 2H/b - 4/(3Pe)$. This formula suggests the diffusion layer thickness is affected by advection, diffusion, cell size, and the porosity and specific area of the electrode. To further understand the dominant control of the limiting current density, we consider two special situations: $Pe \ll 2H/b$ and $Pe \gg 2H/b$. The formula of k_m^* can be reduced to $k_m^* = \frac{u_0 b}{2H}$ for the former scenario and $k_m^* = \frac{D_2}{(5/16 - 2\gamma)b}$ for the latter scenario, which is equivalent to $\delta_d = 2H/Pe$ and $\delta_d = (5/16 - 2\gamma)b \approx 0.25b$ for the two scenarios, respectively. These results suggest that both advection control (u_0) and diffusion control (D_2) are possible and affected by the micro-channel size, which partially explains the reasoning of previous assumptions for deriving formulas for limiting current density. Especially, the diffusion layer thickness in a diffusion control scenario is close to those predicted using an experimentally fitted model which shows

$\delta_d = b/(2+1.534Re^{0.912})$ with $0.3 < Re < 2.4$ [44]. Nevertheless, we have to mention that a combined control from advection and diffusion is more likely to occur for a realistic battery because Pe and H/b likely are of the same order for an actual electrode (Fig. 3b). Experiments on VRFB show that $I_c = k_m^* F c_{23}^0 \text{SoC}$ with $k_m^* = G(\xi) u_0$ [13]. Here ξ denotes a stoichiometric ratio and $G(\xi)$ is a fitted polynomial formula based on the experiment data. The stoichiometric ratio, defined as the ratio of an actual flow rate to a theoretical flow rate that supports a desired cell current [45,46], can be quantified by $\xi = \text{SoC} \frac{\epsilon}{A_s H} I_{cu}^{-1} = \frac{b}{2nH} \frac{F u_0}{I} c_{23}^0 \text{SoC}$ with $n = 1$ and $n = 2$ for strip and grid configuration, respectively (see derivations in Appendix A.1). Ref. [47] argued that the SoC should be a minimum state of charge and suggested a value of 20%. Using such information and the parameters in PNNL experiments (Table 1), the stoichiometric ratio is $\xi = 12.9$ for the experimental setups and such a value results in $G(\xi) = 0.01$ according to Equation (15) in Ref. [13]. By further checking the results of Ref. [13], the function $G(\xi)$ approaches a constant (about 0.056) when the stoichiometric ratio is small, e.g., $\xi < 1$. Note that a small stoichiometric ratio is equivalent to a low flow velocity, therefore such information means a linear relationship between the mass transfer and the flow velocity could be observed. In other words, the mass transfer (and the limiting current density) is controlled by the stoichiometric availability at very low flow velocity, which confirms the conclusion by Refs. [30,35]. This has important implications for estimating the limiting current density in RFBs with flow-by channels (Fig. 1e), where the average microchannel flow velocity is much smaller than that in the flow-through channels [35,38]. On the other hand, a higher flow velocity means the mass transfer (and limiting current density) depends on flow velocity, limiting current density, total active species concentration, electrode porosity, and specific area, which may be mathematically formulated as Equation (12). This formula means a limiting current density can be determined by solving such an equation for a given set of parameters.

$$I_c = G(u_0, I_c; c_{23}^0, \text{SoC}, \epsilon, A_s) \quad (12)$$

5.2. Effects of current density

Fig. 4 shows the over-potential along flow direction under three current densities and two SoCs. In general, the result shows that the over-potential at low SoC (0.3) behaves differently from that at the initial discharge stage (SoC = 0.75) and such a difference is amplified at high current density (10 A/m^2). Firstly, the variation in over-potential along the channel is higher at low SoC than that at high SoC. Specifically, the relative ratio of the difference in over-potential between the channel outlet (η_1^o) and the entrance (η_1^i) to channel average (η_1^{av}) overpotential, defined as $r_{io} = \left| \frac{\eta_1^o - \eta_1^i}{\eta_1^{av}} \right| \times 100\%$, is 2.1%, 17.6%, and 123.5% at current density 1 A/m^2 , 5 A/m^2 , and 10 A/m^2 at low SoC, however, is less than 6.4% for the three current densities at the high SoC. Secondly, it is observed that over-potential approximately linearly increases with

current density at the low current density and high SoC. Particularly, the channel average over-potential increases from 3.2 mV to 17.8 mV with current density increasing from 1 A/m^2 to 5 A/m^2 at low SoC and increases from 3.3 mV to 15.1 mV to 28.0 mV with current density increasing from 1 A/m^2 to 5 A/m^2 to 10 A/m^2 at high SoC, respectively. The third difference is that the over-potential predicted by our model is higher than that predicted by a 0D model at low SoC, while lower than that at a high SoC, and their difference is significant at low SOC and high current density.

The above differences can be generally explained by the interface reaction kinetics and mass transport from advection and diffusion. The underlying mechanism is about providing a certain amount of energy (equivalent to potential) that is used to overcome the energy losses from charge and mass transfer during the reaction. For an ideal situation where the current density and the free energy difference between reactants are zero, i.e., $I = 0$ and $c_3^w/c_2^w = 1$, the reaction system has the minimum potential E_1^0 and thus no extra energy is required to sustain such a state. This situation means the over-potential $\eta_1^w = 0$ does not exist but is an important reference point for understanding an actual VRFB. First, without considering the current density, a difference in the concentration of reactants, i.e., $c_3^w/c_2^w \neq 1$, means an energy barrier exists and certain energy is required to sustain an equilibrium state. The Nernst equation shows that such an energy is directly related to the reaction quotient, defined as $\lambda = c_3^w/c_2^w$, and can be quantified by $E_{eq} - E_1^0 = \frac{1}{f} \ln \left(\frac{c_3^w}{c_2^w} \right)$. Further, though the net current density (I) is zero at an equilibrium state, an exchange current still exists from both the forward and backward reactions despite a zero net effect. Such an exchange current is proportional to the standard reaction rate constant (k_1), the concentration of oxidant (c_3^w), and the energy barrier, which can be represented by $i_0 = k_1 c_3^w e^{-af(E_{eq} - E_1^0)}$ [40]. By replacing $E_{eq} - E_1^0$ with $\frac{1}{f} \ln \left(\frac{c_3^w}{c_2^w} \right)$, the exchange current is reformulated as $i_0 = k_1 c_3^w \left(\frac{c_3^w}{c_2^w} \right)^{-\alpha}$. For an actual VRFB, the current density is different from such an exchange current density, but determined by the amount of energy provided from an external electronic field. For example, to sustain an interface current density I , an external potential E has to be provided to overcome both the minimum potential and the potential difference in reactants. The net current from the forward (i_f) and backward (i_b) reactions can be quantified by $I = i_f - i_b = F k_1 c_3^w \left(\frac{c_3^w}{c_2^w} \right)^{-\alpha} [e^{(1-\alpha)f\eta_1^w} - e^{-af\eta_1^w}]$ [40] with $\eta_1^w = E - E_1^0 - \frac{1}{f} \ln \left(\frac{c_3^w}{c_2^w} \right)$. From such a formula, it is clear that the over-potential depends on two factors: the reaction quotient ($\lambda = c_3^w/c_2^w$) and the desired current density I . Note that we assume a uniform current density along flow direction in this work; therefore, the current density does not directly contribute to the variation in over-potential. By contrast, the over-potential variations are directly attributed to the variations in species concentration due to advection and diffusion. Recalling that the

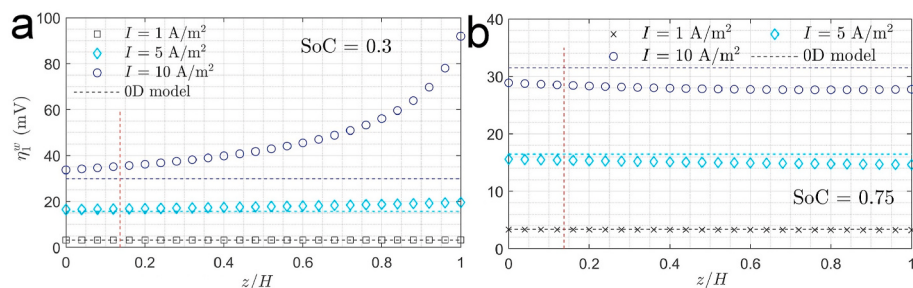


Fig. 4. Effects of current density on the wall over-potential along flow direction under different SoC. The over-potential is calculated with $c_{23}^0 = 1080 \text{ mol/m}^3$ [1] and other parameters are identical to those used in the base case (Table 1 column 3) except for those marked on each figure. Horizontal and vertical dashed lines represent over-potential calculated from the 0D model (Equation (10)) and concentration entrance length, respectively.

minimum over-potential occurs at $\lambda = 1$ and $I = 0$, the different behaviors observed above can be explained by three situations: $\lambda < 1$, $\lambda = 1$, and $\lambda > 1$ for a given current density I . In addition, the mass conservation between the reactants means $\lambda = \frac{1}{c_2^w} - 1$.

With this information, the effects of current density on over-potential can be explained as follows. Firstly, the increasing trend in over-potential along the flow direction (z) at a low SoC (Fig. 4a) occurs because the reaction quotient $\lambda > 1$ and increases along the flow direction. This means that the reaction process becomes increasingly far away from the minimum free energy status with increasing z coordinate, and thus increasingly high over-potential (energy) is required to overcome the energy barrier to reach the desired current density. By contrast, the reaction quotient $\lambda < 1$ and increases with increasing z at a high SoC (Fig. 4b). This means that the reaction process is approaching the minimum free energy status ($\lambda = 1$) from the entrance to the outlet, and thus increasingly low over-potential (energy) is required to overcome the energy barrier. Secondly, the larger variation in over-potential is attributed to advection and diffusion. For a transfer coefficient 0.5, the forward and backward reactions are symmetrical without considering mass transport from advection and diffusion, which can be easily proved by the mathematically symmetric expression of over-potential in Equation (10). In other words, the over-potential is the same at a SoC and 1 - SoC. However, this is not true for the over-potential affected by advection and diffusion. For example, for two given SoCs 0.3 and 0.7, the actual concentration used in Equation (7) (neglecting the last term due to a small value) is $c_2^{w*1} = 0.3 - (5/16 - 2\gamma)I_{cd} - 2zI_{cu}/b$ and $c_2^{w*2} = 0.7 - (5/16 - 2\gamma)I_{cd} - 2zI_{cu}/b$, respectively. The symmetry of Equation (8) means the over-potential at a concentration $c_2^{w*1s} = 1 - c_2^{w*1} = 0.7 + (5/16 - 2\gamma)I_{cd} + 2zI_{cu}/b$ is identical to that at c_2^{w*1} . As the concentration is inversely proportional to the reaction quotient, $c_2^{w*1s} > c_2^{w*2} > 0.5$ means that the reaction process with c_2^{w*1s} (equivalent to c_2^{w*1}) is further away from the minimum free energy status compared to that with a concentration c_2^{w*2} . As c_2^{w*1} and c_2^{w*2} denote the actual concentration at given SoCs 0.3 and 0.7, the above information suggests a larger over-potential is required for the lower SoC to sustain a given current density. The above analyses demonstrate it is the diffusion (I_{cd}) and advection (I_{cu}) that result in the difference and a higher current density enhanced such a difference. Thirdly, the over-potential increasing with increasing current density is attributed to more energy required to overcome the energy barrier to sustain a higher current density. Fourthly, the linear relationship between over-potential and current density at low current densities is attributed to negligible mass transfer resistance, i.e., $I_{cu} \approx 0$ and $I_{cd} \approx 0$. Without the mass transfer resistance, the battery behaves like a pure resistance circuit which is characterized with a linear potential-current relationship [40]. By neglecting the mass transfer effects, the wall concentration (Equation (7)) is reduced to SoC and the wall over-potential (Equation (8)) is reduced to $\eta_1^{wl} = \frac{RT}{k_1 F^2} \frac{I}{\sqrt{c_2^0 c_3^0}}$. For a given SoC, such a formula is equivalent to $\eta_1^{wl} = \frac{RT}{k_1 F^2} \frac{I_t}{c_{23}^0} [\text{SoC}(1 - \text{SoC})]^{-1/2}$ and thus the charge-transfer resistance can be calculated by $R_{ct} = \eta_1^{wl}/I_t = \frac{RT/F}{F c_{23}^0 k_1 A_s B H L_e} [\text{SoC}(1 - \text{SoC})]^{-1/2}$. This formula reveals that the non-dimensional number I_{ek} ($= \frac{I}{F c_{23}^0 k_1}$) is a metric for quantifying charge-transfer resistance. Lastly, a higher over-potential observed in our model than that from the 0D model at a low SoC (Fig. 4a) is attributed to the advection and diffusion effects, which reduce the wall concentration, increase the reaction quotient, produce a larger deviation ($\lambda > 1$) from the minimum free energy state, and result in larger over-potential. A lower over-potential from our model than that from the 0D model at a higher SoC (Fig. 4b) can be explained similarly.

5.3. Effects of flow velocity

Due to the importance of advection and diffusion, this section considers a realistic battery with a pumping rate $\omega = 60 \text{ mL/min}$ [1,21], cell width $B = 0.1 \text{ m}$ [1], cell thickness $L_e = 4 \text{ mm}$, porosity $\varepsilon = 0.926$, and specific area $A_s = 3.75e4 \text{ m}^2/\text{m}^3$ [17]. With this information, the average pore size is estimated as $b = 4\varepsilon/A_s \approx 100 \mu\text{m}$, and the average flow velocity is estimated as $u_0 = \omega/(e L_e B) = 2.7 \text{ mm/s}$. Note that the grid configuration is used to approximate an actual electrode structure and the estimated pore size and flow velocity is close to those measured and modeled using an actual electrode [17]. Therefore, we choose three velocities (1, 5, and 25 mm/s) to study the effect of flow velocity on over-potential.

Fig. 5 shows the variation of wall over-potential along the channel at three velocities under two current densities and two SoCs. In general, the results show that the variation in over-potential is negligible ($r_{lo} \leq 2.4\%$) at low current density (Fig. 5a,b). At high current density, the variation is also negligible ($r_{lo} \leq 4.0\%$) when the flow velocity is high ($\geq 5 \text{ mm/s}$); however, it is significant ($r_{lo} = 37.7\%$ at SoC = 0.3 and $r_{lo} = 11.6\%$ at SoC = 0.75) at low flow velocity (1 mm/s) and high current density. Besides, a comparison between our model (lines with symbols) with the 0D model (horizontal dashed lines) shows that the 0D model predicts lower over-potential than our model at low SoC and higher values than our models at high SoC. More specifically, the maximum difference, i.e., r_{02} (Supplementary information Text S1), in over-potential between the two models is less than 4.8% at low current density and high flow velocity (Fig. 5a-b and $u_0 \leq 5 \text{ mm/s}$ in Fig. 5d), but about 11.8%~45% at low flow velocity and high current density (velocity 1 mm/s in Fig. 5c-d).

The small variation in over-potential at a low current density is attributed to the negligible mass-transfer resistance (I_{cd} and I_{cu}), which is proportional to the current density. At a high current density, the variation in over-potential could still be small if the flow velocity is high enough (blue star in Fig. 5c and d). Physically, a high flow velocity means the transport of reactants is easier and thus the concentration is more uniform along the flow direction. This can be mathematically proven by a small value of I_{cu} at a sufficiently high velocity and thus wall concentration (Equation (7)) has little variation along z . As the reaction quotient depends on concentration, a more uniform concentration at a sufficiently high flow velocity means the potential (energy) required to sustain a given current density is more uniform along the z -direction. By contrast, the transport resistance due to advection at low flow velocity is higher, which results in a much larger concentration gradient along the flow direction. This further means the reaction quotient experiences a larger variation along the flow direction and thus generates larger differences in the over-potential along z (see red cross lines in Fig. 5). The higher over-potential predicted in our model, compared to that from the 0D model at a low SoC (Fig. 5a,c), is caused by the advection and diffusion as explained in Section 5.2. The lower over-potential predicted in our model at a high SoC (Fig. 5b,d) can be explained similarly. And such a difference becomes larger (Fig. 5 red cross lines and black dashed lines) when the advection effect becomes more important, which essentially corresponds to low velocity and thus a higher I_{cu} value. This likely has important implications for velocity optimization for real VRFBs. Firstly, much lower flow velocities (0.264 mm/s ~ 1.3 mm/s) have been reported in actual electrodes [17], which means that larger mass-transport resistance may be common in actual VRFBs; secondly, though using a higher flow velocity is possible to reduce the mass-transport resistance, it requires more pump energy to balance a higher pressure drop induced by the high flow velocity. Various flow-through and flow-by channels have been designed to reduce the pressure, however, this can result in lower flow velocity due to increased flow resistance from these complex channels. Considering these contradictory factors, the analyses here may provide a clue to better designs for flow channels. A potential direction is to replace the average flow velocity u_0 with an existing analytical solution for flow field [30] or with

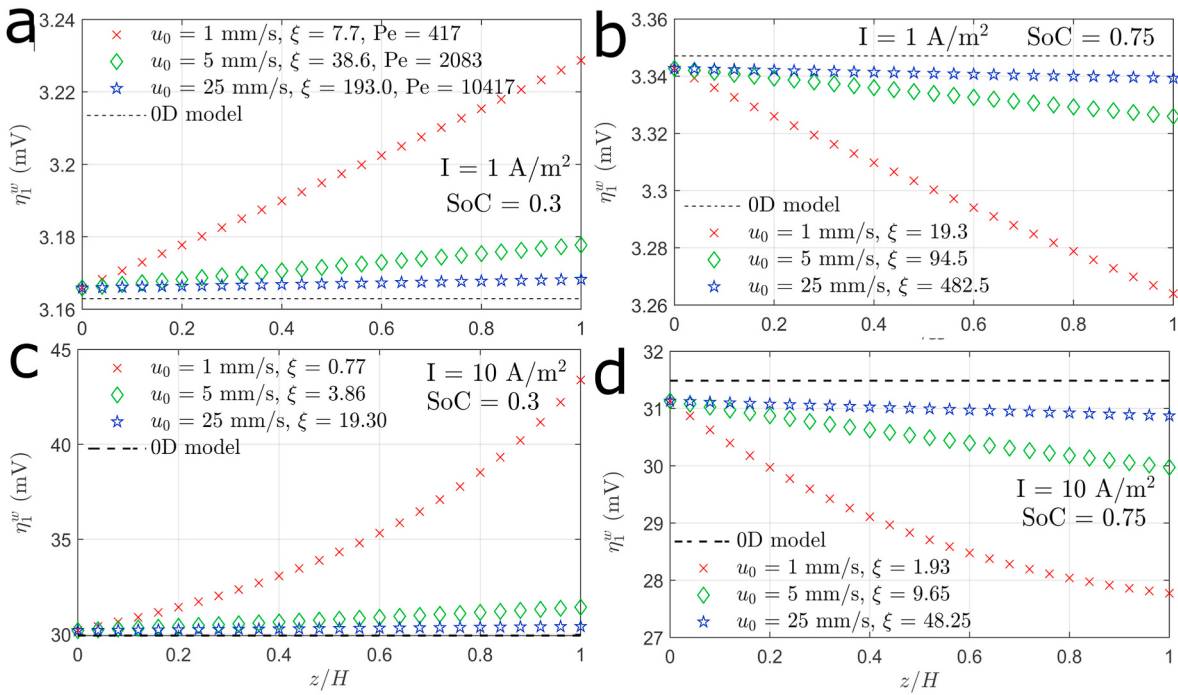


Fig. 5. Distribution of wall over-potential along flow direction at three flow velocities under two current densities and two SoCs. Over-potential is calculated using $b = 100 \mu\text{m}$, $c_{23}^0 = 1080 \text{ mol/m}^3$, and other parameters are identical to the base case (Table 1 column 3). The stoichiometric ratio and Peclet number are denoted by ξ and Pe . The stoichiometric ratio is calculated using $\xi = \epsilon/(A_s H I_{cu}) \text{SoC}$. Peclet numbers in b-d are identical to that in a.

velocity distribution from 3D computational fluid dynamic simulations.

Fig. 5 also shows an increasing trend in over-potential along the flow direction at low SoC (Fig. 5a,c) and a decreasing trend at high SoC (Fig. 5b,d). This is similar to the spatial variation trend observed in Fig. 4a and b, and both trends share the same underlying mechanisms as discussed in Section 5.2.

In addition to flow velocity, other parameters such as standard reaction rate constant, active ion diffusivity, total active species concentration, and microchannel width also affect the distribution of over-potential. Their effects on over-potential are discussed in Supplementary Information S1 – S4.

6. Conclusion

This work proposed analytical solutions to active species concentration and over-potential within a RFB cell. Specifically, analytical solutions for centerline and wall concentration, and wall over-potential are given as Equations (6)–(8), respectively. These solutions agree well with results from a finite element numerical model and a calibrated 0D model, and demonstrate better capability in predicting over-potential variations under high current density, low flow velocity, and low diffusivity scenarios compared to a 0D model. The analysis of the over-potential - SoC curve shows that its minimum value (Equation (9)) is solely determined by a charge-transfer resistance related non-dimensional number I_{ck} that depends on standard reaction rate constant and total concentration of active species. In addition, two formulas for limiting current density (Equations (11) and (12)) show their dependencies on flow velocity, diffusivity, and electrode structure as well as total active species concentration and SoC.

The dependencies of over-potential on local current density, flow velocity, standard reaction rate constant, active ion diffusivity, total active species concentration, and electrode structure were also studied. For current density, the results show that over-potential decreases along the flow channel (z) at high SoC while increases with z at low SoC, and are controlled by the combined effects of reaction quotient, charge-transfer and mass-transfer resistances that are enhanced at high

current density. The effects of standard reaction rate constant and total species concentration are similar, both of which show that over-potential decreases with increasing standard rate constant or total concentration and such a decrease is faster at a high standard rate constant. The effects of flow velocity and diffusivity are also similar but more complex and more dependent on SoC. In particular, the over-potential decreases with increasing flow velocity or diffusivity at a low SoC and increases with increasing flow velocity and diffusivity at a high SoC. The microchannel size, determined by electrode porosity, specific area, and pore distribution, has the most complex effects on over-potential. Specifically, an optimal channel size may exist for a given current density, SoC, flow velocity, and diffusivity. The over-potential at such a size behaves differently from those at neighboring sizes. In addition, a smaller channel size may result in significant variations in over-potential along the flow channel. Overall, the complex behaviors in over-potential depend on many different parameters and a comprehensive optimization for these parameters is necessary for the best overall cell performance.

CRediT authorship contribution statement

Yunxiang Chen: Conceptualization, Methodology, Software, Validation, analyses, Investigation, Writing - original draft. **Zhijie Xu:** Conceptualization, Supervision, Project administration, Funding acquisition. **Chao Wang:** Software, and analyses. **Jie Bao:** analyses, discussion, Supervision, Project administration, Funding acquisition, Data curation. **Brian Koeppel:** analyses and discussion. **Litao Yan:** experiments. **Peiyuan Gao:** analyses and discussion. **Wei Wang:** Project administration, Funding acquisition.

Declaration of competing interest

The authors declare that they have no known competing financial interests or personal relationships that could have appeared to influence the work reported in this paper.

Acknowledgments

This research was supported by Energy Storage Materials Initiative (ESMI), which is a Laboratory Directed Research and Development Project at Pacific Northwest National Laboratory (PNNL). PNNL is a

multiprogram national laboratory operated for the U.S. Department of Energy (DOE) by Battelle Memorial Institute under Contract no. DE-AC05-76RL01830. The authors thank the two anonymous reviewers and associate editor for their constructive feedback of this work.

Appendix A. Supplementary mathematical derivations

A.1. Estimation of microchannel size, flow velocity, local current density, and stoichiometric ratio

As we approximate an actual electrode using many microchannels arranged as either a strip or a grid as shown in Fig. 1, the following derivations are developed based on the two approximations. For the strip configuration, we denote the average microchannel size as b , the size of the adjacent solid with b_s , and the number of channels as N . Therefore, we have cell width $B = N(b + b_s)$, electrode porosity $\epsilon = NbH_e/(BHL_e)$, and specific area $A_s = 2NL_eH/(BHL_e)$. Combining the equations for ϵ and A_s , we get $b = 2\epsilon/A_s$. Further, combining the first and the second equation, we have $b_s = b(1/\epsilon - 1) = (2 - 2\epsilon)/A_s$. With b and b_s , the number of channels is estimated by $N = BA_s/2$. As the volumetric flow rate at the inlet is calculated as $\omega = NbL_eu_0$, we can estimate the flow velocity with $u_0 = \omega/(NbL_e) = \omega/(BL_e\epsilon)$. Similarly, the charge conservation of electrons means that $I_t = 2NL_eHI$. Substituting N to such an equation gives $I = I_t/(A_sBHL_e) = I_t/(BH)/(A_sL_e) = I_0/(A_sL_e)$ with I_0 denoting the nominal current density.

For the grid configuration, if denoting the number of channels along cell thickness (x) and width (y) direction by N_x and N_y , then we have $L_e = N_x(b + b_s)$ and $B = N_y(b + b_s)$, which means $BL_e = N_xN_y(b + b_s)^2$. Here each individual channel is assumed as a square channel with identical sizes along x and y directions. With this, the porosity and specific area are calculated by $\epsilon = N_xN_yb^2H/(BHL_e)$ and $A_s = 4bHN_xN_y/(BHL_e)$. From here we have $b = 4\epsilon/A_s$ and $N_xN_y = eBL_e/b^2$. By combining the equation for BL_e and ϵ , we get $BL_e/\epsilon = (b + b_s)^2/b^2BL_e$, and thus the adjacent solid size can be calculated by $b_s = b(\epsilon^{-1/2} - 1) = 4(\sqrt{\epsilon} - \epsilon)/A_s$. As the flow velocity is calculated by $\omega = N_xN_yb^2u_0$, we have $u_0 = \omega/(N_xN_yb^2) = \omega/(BL_e\epsilon)$. Again, the charge conservation of electrons means that $I_t = 4bHN_xN_yI$, which means $I = I_t/(4bHN_xN_y) = I_t/(A_sBHL_e) = I_0/(A_sL_e)$.

The stoichiometric ratio is defined as the ratio of an actual flow rate and the maximum flow rate that the VRFB can consume, which has the form as $\xi = \omega/\omega_{max}$. The maximum flow rate the VRFB can consume is determined by the desired current and the availability of reactants and can be calculated by $\omega_{max} = I_t/(Fc_{23}^0\text{SoC})$ [46]. Substituting the flow velocity and local current density into such a formula gives $\xi = \frac{Fc_{23}^0u_0}{I}\frac{\epsilon}{A_sH}\text{SoC} = e\text{SoC}/(A_sH)I_{cu}^{-1}$. This can be further simplified as $\xi = \frac{b}{2nH}\frac{Fu_0}{I}c_{23}^0\text{SoC}$ with $n = 1$ for strip and $n = 2$ for grid configuration.

A.2. Simplification for governing equation of ionic potential

To evaluate the effective conductivity and source terms for ionic potential, we consider all charged ions in the negative cell including H^+ , V^{2+} , V^{3+} , HSO_4^- , and SO_4^{2-} . For convenience, we mark these ions by 1, 2, 3, 4, and 5, respectively. The mass conservation of the reactants between V^{2+} and V^{3+} means that their summation (c_{23}) is a constant. Using such information and the assumption of identical diffusivity between V^{2+} and V^{3+} , the effective conductivity can be rewritten as Equation (13).

$$k_{eff} = \frac{F^2}{RT} \sum_{j=1,4,5} z_j^2 D_j c_j + \frac{F^2}{RT} z_3^2 D_3 c_{23} + \frac{F^2}{RT} z_2^2 D_2 c_2 \left(1 - \frac{z_3^2}{z_2^2}\right) = k_{eff}^n + k_{eff}^a \quad (13)$$

where k_{eff}^n and k_{eff}^a denote the effective conductivity attributed to non-active and active species. For non-active species in a steady state, their concentrations are always constant which means k_{eff}^n is constant. If defining a ratio of the two contributing parts, we have Equation (14).

$$\alpha_{na} = \left| \frac{k_{eff}^a}{k_{eff}^n} \right| \leq \frac{z_3^2 - z_2^2}{\sum_{j=1,4,5} z_j^2 (D_j/D_2) (c_j/c_{23}) + z_3^2} \quad (14)$$

Note that the valences of the charged ions for H^+ , V^{2+} , V^{3+} , HSO_4^- , and SO_4^{2-} are 1, 2, 3, -1, and -2; and that the concentrations of proton and hydrogen sulfate ion are usually higher than the total concentration of active species, i.e., $c_j > c_{23}$ [28,38], therefore, the ratio $\alpha_{na} < 5/[(D_1 + D_4 + 4D_5)/D_2 + 9]$. Measurements further show that the diffusivities of proton (D_1), hydrogen sulfate ion (D_4), and the sulfate (D_5) in the electrolyte are much higher than the diffusivity of V^{2+} . For example, $D_1 = 9.31 \times 10^{-9} \text{ m}^2/\text{s}$ [34], $D_4 = 1.33 \times 10^{-9} \text{ m}^2/\text{s}$ [48], and $D_5 = 1.07 \times 10^{-9} \text{ m}^2/\text{s}$ [48] while $D_2 = 2.4 \times 10^{-10} \text{ m}^2/\text{s}$ [49]. This means that the ratio α_{na} is less or much less than 7% for an actual VRFB electrolyte and it is reasonable to simplify the effective conductivity to the non-active part which is constant at a steady state.

For the source terms contributing to the ionic potential, the assumption of equivalent diffusivities for V^{2+} and V^{3+} means that $z_2 D_2 c_2 + z_3 D_3 c_3 = z_2 D_2 c_2 + z_3 D_2 c_3$. The electroneutrality of the electrolyte further means $z_2 c_2 + z_3 c_3 = -\sum_{j=1,4,5} z_j c_j$. Using these conditions, the source terms can be rewritten as Equation (15).

$$\nabla \cdot \left(F \sum_{j=1,4,5} z_j D_j \nabla c_j \right) = \nabla^2 \left[F \sum_{j=1,4,5} z_j (D_j - D_2) c_j \right] \quad (15)$$

Note that the concentrations of non-active species ($j = 1, 4$, and 5) are constant at a steady state and therefore the source terms can be reduced to 0 at a steady state.

A.3: Reduced boundary method

To reduce the mathematical complexity, we transform Equation (1) into a cylindrical coordinate system as shown in Equation (16). For

convenience, we represent $c_2^{c,n} = \frac{\partial^n c_2}{\partial r^n}|_{r=0}$ and $c_2^{w,n} = \frac{\partial^n c_2}{\partial r^n}|_{r=a}$ with $a = b/2$ denoting the radius of a microchannel. Therefore, the boundary conditions discussed in Section 2.2 for c_2 at the wall and centerline can be represented by $c_2^{w,1} = -I/(FD_2)$ and $\partial c_2^c / \partial z = 0$, respectively.

$$\frac{\partial c_2}{\partial t} + u(r) \frac{\partial c_2}{\partial z} = D_2 \left(\frac{\partial^2 c_2}{\partial z^2} + \frac{d}{r} \frac{\partial c_2}{\partial r} + \frac{\partial^2 c_2}{\partial r^2} \right) \quad (16)$$

For fully developed flow, velocity $u(r)$ is symmetric along r direction. In addition, the boundary condition for c_2 is symmetric at the two walls. These conditions mean the solution to c_2 is symmetric and thus the odd order derivatives of c_2 with respect to r at the centerline are zero, i.e., $c_2^{c,2i+1} = 0$ ($i = 0, 1, 2, \dots$). Applying Equation (16) at $r = 0$ with the symmetric condition gives Equation (17) for centerline concentration c_2^c .

$$\frac{\partial c_2^c}{\partial t} + \frac{d+3}{2} u_0 \frac{\partial c_2^c}{\partial z} - D_2 \frac{\partial^2 c_2^c}{\partial z^2} = D_2(d+1)c_2^{c,2} \quad (17)$$

Equation (17) requires to link $c_2^{c,2}$ to the wall boundary condition $c_2^{w,1}$ in order to derive a solution to c_2^c . In this work, we approximate a concentration at any location by a summation of a series of polynomials as shown in Equation (18).

$$c_2(x, r, t) = c_2^c + \sum_{i=1}^{+\infty} \frac{r^{2i}}{(2i)!} c_2^{c,2i} \quad (18)$$

where $c_2^{c,2i}$ denotes even order derivatives with respect to r at the centerline.

We then apply Equation (18) to calculate the wall concentration c_2^w and the first and second order derivatives of c_2 with respect to r at the wall as Equations (19)–(21).

$$c_2^w = c_2^c + \frac{a^2}{2} c_2^{c,2} + \frac{a^4}{24} c_2^{c,4} + \sum_{i=3}^{+\infty} \frac{a^{2i}}{(2i)!} c_2^{c,2i} \quad (19)$$

$$c_2^{w,1} = ac_2^{c,2} + \frac{a^3}{6} c_2^{c,4} + \sum_{i=3}^{+\infty} \frac{a^{2i-1}}{(2i-1)!} c_2^{c,2i} \quad (20)$$

$$c_2^{w,2} = c_2^{c,2} + \frac{a^2}{2} c_2^{c,4} + \sum_{i=3}^{+\infty} \frac{a^{2i-2}}{(2i-2)!} c_2^{c,2i} \quad (21)$$

By dropping the terms with order higher than 5 in Equations (20) and (21) and solving the resulting linear equations, we obtain Equations (22) and (23).

$$c_2^{c,2} = \frac{3}{2a} c_2^{w,1} - \frac{1}{2} c_2^{w,2} \quad (22)$$

$$c_2^{c,4} = -\frac{3}{a^3} c_2^{w,1} + \frac{3}{a^2} c_2^{w,2} \quad (23)$$

Note that $c_2^{w,1} = -I/(FD_2)$ is a constant and thus $c_2^{w,2} = 0$, which further gives $c_2^{c,2} = -\frac{3I}{2aFD_2}$ and $c_2^{c,4} = \frac{3I}{a^2FD_2}$. Substituting $c_2^{c,2}$ into Equation (17) gives Equation (24).

$$\frac{\partial c_2^c}{\partial t} + \frac{d+3}{2} u_0 \frac{\partial c_2^c}{\partial z} - D_2 \frac{\partial^2 c_2^c}{\partial z^2} = -\frac{3(d+1)I}{2Fa} \quad (24)$$

As discussed in Section 2.2, the boundary condition for centerline concentration is $\frac{\partial c_2^c}{\partial z}|_{z=H} = 0$ and $c_2^c|_{z=z_e} = c_2^e$. Therefore, the analytical solution to Equation (24) can be derived as Equation (25) with $b = 2a$.

$$c_2^c = c_2^e - \frac{6(d+1)}{d+3} \frac{I}{Fu_0 b} (z - z_e) - \frac{12(d+1)}{(d+3)^2} \frac{ID_2}{Fu_0^2 b} \left[e^{\frac{d+3}{2} \frac{u_0}{D_2} (z_e - H)} - e^{\frac{d+3}{2} \frac{u_0}{D_2} (z - H)} \right] \quad (25)$$

Substituting Equations (22) and (23) into Equation (21) and Equation (18) gives a solution to wall concentration and concentration at all locations as Equations (26) and (27), respectively.

$$c_2^w = c_2^c - \frac{5}{16} \frac{Ib}{FD_2} \quad (26)$$

$$c_2 = c_2^c - \frac{3}{8} \frac{Ib}{FD_2} \left(\frac{r}{a} \right)^2 + \frac{1}{16} \frac{Ib}{FD_2} \left(\frac{r}{a} \right)^4 \quad (27)$$

Defining four non-dimensional parameters: SoC = $\frac{c_2^i}{c_{23}^0}$, $I_{cu} = \frac{I}{Fu_0 c_{23}^0}$, $Pe = \frac{u_0 b}{D_2}$, $I_{cd} = \frac{Ib}{FD_2 c_{23}^0}$, and $I_{ck} = \frac{I}{Fk_1 c_{23}^0}$, Equations (25) and (26) can be rewritten as Equations (6) and (7). The wall over-potential η_1^w can be also be derived as Equation (8) with the solution of c_2^{w*} .

Appendix B. Nomenclature

α	Transfer coefficient
α_{na}	Ratio of active conductivity to non-active conductivity

L_e	Flow cell length (m)
H	Flow cell height (m)
B	Flow cell width (m)
b	Pore size or microchannel size (m)
ε	Electrode porosity
A_s	Electrode specific area ($\text{m}^2 \text{ m}^{-3}$)
b_s	Average fiber size (m)
x	Spatial coordinate along channel length direction (m)
y	Spatial coordinate along channel width direction (m)
z	Spatial coordinate along channel height direction (m)
\vec{U}	Electrolyte flow velocity vector (m s^{-1})
u	Electrolyte flow velocity component along channel height direction (m s^{-1})
u_m	Channel centerline velocity (m s^{-1})
u_0	Channel cross-sectional average velocity (m s^{-1})
r	Channel radial coordinate (m)
d	Channel shape parameter, 0 and 1 denote square and circular
c_2	Concentration of V^{2+} (mol m^{-3})
c_3	Concentration of V^{3+} (mol m^{-3})
t	time (s)
D_2	Diffusivity of V^{2+} ($\text{m}^2 \text{ s}^{-1}$)
D_3	Diffusivity of V^{3+} ($\text{m}^2 \text{ s}^{-1}$)
ϕ_e	Ionic potential in electrolyte (V)
k_{eff}	Effective conductivity (S m^{-1})
F	Faraday constant, 96485.33 C mol $^{-1}$
z_j	Valence of species j
D_j	Diffusivity of species j ($\text{m}^2 \text{ s}^{-1}$)
c_j	Concentration of species j (mol m^{-3})
R	Ideal gas constant, 8.314 J mol $^{-1}$ K $^{-1}$
$S(x)$	Ionic flux gradient along cell thickness direction
I	Local wall current density (A m^{-2})
i_w	Current density at the channel interface (A m^{-2})
\vec{J}_2	Mass flux of V^{2+} at channel interface ($\text{mol m}^{-2} \text{ s}^{-1}$)
\vec{J}_3	Mass flux of V^{3+} at channel interface ($\text{mol m}^{-2} \text{ s}^{-1}$)
\vec{n}	Interface surface normal direction
i_0	Exchange current at interface ($\text{mol m}^{-2} \text{ s}^{-1}$)
f	A constant defined by $f = F/(RT)$, 38.92 V $^{-1}$
η_1^w	Wall over-potential (V)
k_1	Standard reaction rate constant for negative cell (m s^{-1})
c_2^w	Concentration of V^{2+} at the wall (mol m^{-3})
c_3^w	Concentration of V^{3+} at the wall (mol m^{-3})
ϕ_s^w	Electronic potential at the wall (V)
ϕ_e^w	Ionic potential at the wall (V)
E_1^0	Standard potential between V^{2+} and V^{3+} (V)
I_t	Total current applied to flow cell (A)
I_0	Nominal current density (A m^{-2})
N	Number of microchannels in the electrode
c_2^i	Initial concentration of V^{2+} (mol m^{-3})
z_e	Entrance length of concentration (m)
γ	Concentration entrance length constant, 0.033
Pe	Peclet number
c_{23}	Total concentration of V^{2+} and V^{3+} (mol m^{-3})
c_3^i	Initial concentration of V^{3+} (mol m^{-3})
c_{23}^i	Total concentration of V^{2+} and V^{3+} at channel inlet (mol m^{-3})
c_{23}^0	Initial total concentration of V^{2+} and V^{3+} (mol m^{-3})
c_2^*	Non-dimensional centerline concentration of V^{2+}
c_3^*	Non-dimensional centerline concentration of V^{3+}
c_2^{w*}	Non-dimensional wall concentration of V^{2+}
c_3^{w*}	Non-dimensional wall concentration of V^{3+}
SoC	State of charge
I_{cu}	Relative importance of current density to advection
I_{cd}	Relative importance of current density to diffusion
I_{ck}	Relative importance of current density to reaction
η_1^{wc}	Minimum over-potential in potential - SoC curve (V)

η_1^{w0}	Over-potential calculated from a 0D model (V)
I_c	Local limiting current density ($A\ m^{-2}$)
I_{c0}	Nominal limiting current density ($A\ m^{-2}$)
k_m^*	Lumped mass transfer coefficient ($m\ s^{-1}$)
k_m	Mass transfer coefficient ($m\ s^{-1}$)
u_f	Cross-sectional velocity in porous medium ($m\ s^{-1}$)
Q_p	Flow rate penetrating from electrolyte to electrode ($m^3\ s^{-1}$)
c_b	Bulk concentration ($mol\ m^{-3}$)
c_0	Interface concentration ($mol\ m^{-3}$)
δ_d	Diffusion layer thickness (m)
Re	Reynolds number
ξ	Stoichiometric ratio
$G(\xi)$	Fitted polynomial function for mass transfer
n	Electrode configuration parameter
η_1^o	Over-potential at channel outlet (V)
η_1^i	Over-potential at channel entrance (V)
η_1^{av}	Average over-potential along the channel (V)
r_{io}	Relative ratio of over-potential difference to the average potential
λ	Reaction quotient
E_{eq}	Equilibrium potential (V)
i_f	Current density from forward reaction ($A\ m^{-2}$)
i_b	Current density from backward reaction ($A\ m^{-2}$)
η_1^{wl}	Over-potential at low current density (V)
R_{ct}	Charge-transfer resistance ($S\ m^{-1}$)
r_{02}	Relative over-potential difference between a 2D model and a 0D model
ω	Pumping rate ($L\ s^{-1}$)
v_{net}	Net reaction conversion ($mol\ m^{-2}\ s^{-1}$)
v_f	Forward reaction conversion ($mol\ m^{-2}\ s^{-1}$)
v_b	Backward reaction conversion ($mol\ m^{-2}\ s^{-1}$)
C_O^w	Oxidant concentration at interface ($mol\ m^{-3}$)
C_R^w	Reductant concentration at interface ($mol\ m^{-3}$)
k_f	Forward reaction rate constant ($m\ s^{-1}$)
k_b	Backward reaction rate constant ($m\ s^{-1}$)
z_m	Location of local minimum over-potential (m)
a	Radius of microchannel (m)
N_x	Number of microchannels in cell thickness direction
N_y	Number of microchannels in cell width direction
ω_{max}	Maximum flow rate in VRFB ($L\ s^{-1}$)
k_{eff}^a	Effective conductivity from active species ($S\ m^{-1}$)
k_{eff}^n	Effective conductivity from non-active species ($S\ m^{-1}$)
D_1	Diffusivity of H^+ ($m^2\ s^{-1}$)
D_4	Diffusivity of HSO_4^- ($m^2\ s^{-1}$)
D_5	Diffusivity of SO_4^{2-} ($m^2\ s^{-1}$)
RFB	Redox flow battery
$VRFB$	Vanadium redox flow battery

Disclaimer

The work from Chao Wang was conducted during this previous employment at Pacific Northwest National Laboratory. Framatome Inc. is his current employment and is not involved in any of this work in any way and therefore holds no responsibility or liability for the accuracy or the completeness of the information contained in this paper.

Appendix C. Supplementary data

Supplementary data to this article can be found online at <https://doi.org/10.1016/j.jpowsour.2020.228817>.

References

- [1] A.A. Shah, M.J. Watt-Smith, F.C. Walsh, A dynamic performance model for redox-flow batteries involving soluble species, *Electrochim. Acta* 53 (27) (2008) 8087–8100, <https://doi.org/10.1016/j.electacta.2008.05.067>.
- [2] G. Kean, A.A. Shah, F.C. Walsh, Development of the all-vanadium redox flow battery for energy storage: a review of technological, financial and policy aspects, *Int. J. Energy Res.* 36 (2012) 1105–1120, <https://doi.org/10.1002/er.1863>.
- [3] X. Zhou, T. Zhao, L. An, Y. Zeng, L. Wei, Critical transport issues for improving the performance of aqueous redox flow batteries, *J. Power Sources* 339 (2017) 1–12, <https://doi.org/10.1016/j.jpowsour.2016.11.040>.
- [4] P. Leung, A.A. Shah, L. Sanz, C. Flox, J.R. Morante, Q. Xu, M.R. Mohamed, C. Ponce de León, F.C. Walsh, Recent developments in organic redox flow batteries: a critical review, *J. Power Sources* 360 (2017) 243–283, <https://doi.org/10.1016/j.jpowsour.2017.05.057>.
- [5] R.F. Service, Tanks for the batteries, *Science* 344 (6182) (2014) 352–354, <https://doi.org/10.1126/science.344.6182.352>.

- [6] K. Mongird, V. Viswanathan V., P. Balducci J., Md Jan Alam E., V. Fotedar, V. Koritarov S., B. Hadjerioua, Energy storage technology and cost characterization report, Tech. Rep., PNNL-28866, US Department of Energy, 2019, <https://doi.org/10.2172/1573487>.
- [7] S. Kim, E. Thomsen, G. Xia, Z. Nie, J. Bao, K. Recknagle, W. Wang, V. Viswanathan, Q. Luo, X. Wei, A. Crawford, G. Coffey, G. Maupin, V. Sprenkle, 1 kW/1 kWh advanced vanadium redox flow battery utilizing mixed acid electrolytes, *J. Power Sources* 237 (2013) 300–309, <https://doi.org/10.1016/j.jpowsour.2013.02.045>.
- [8] A.Z. Weber, M.M. Mench, J.P. Meyers, P.N. Ross, J.T. Gostick, Q. Liu, Redox flow batteries: a review, *J. Appl. Electrochem.* 41 (2011) 1137–1164, <https://doi.org/10.1007/s10800-011-0348-2>.
- [9] J. Kim, H. Park, Electrokinetic parameters of a vanadium redox flow battery with varying temperature and electrolyte flow rate, *Renew. Energy* 138 (2019) 284–291, <https://doi.org/10.1016/j.renene.2019.01.102>.
- [10] M. Skyllas-Kazacos, F. Grossmith, Efficient vanadium redox flow cell, *J. Electrochem. Soc.* 134 (12) (1987) 2950–2953, <https://doi.org/10.1149/1.2100321>.
- [11] R. Carta, S. Palmas, A.M. Polcaro, G. Tola, Behaviour of a carbon felt flow by electrodes Part I: mass transfer characteristics, *J. Appl. Electrochem.* 21 (1991) 793–798, <https://doi.org/10.1007/BF01402816>.
- [12] D. Aaron, C.N. Sun, M. Bright, A.B. Papandrew, M.M. Mench, T.A. Zawodzinski, In situ kinetics studies in all-vanadium redox flow batteries, *ECS Electrochemistry Letters* 2 (3) (2013) A29–A31, <https://doi.org/10.1149/2.001303ecl>.
- [13] J.Y. Chen, C.L. Hsieh, N.Y. Hsu, Y.S. Chou, Y.S. Chen, Determining the limiting current density of vanadium redox flow batteries, *Energies* 7 (2014) 5863–5873, <https://doi.org/10.3390/en7095863>.
- [14] R.M. Darling, M.L. Perry, The influence of electrode and channel configurations on flow battery performance, *J. Electrochem. Soc.* 161 (9) (2014) A1381–A1387, <https://doi.org/10.1149/2.0941409jes>.
- [15] Y.A. Gandomi, D.S. Aaron, T.A. Zawodzinski, M.M. Mench, In situ potential distribution measurement and validated model for all-vanadium redox flow battery, *J. Electrochem. Soc.* 163 (1) (2016) A5188–A5201, <https://doi.org/10.1149/2.0211601jes>.
- [16] A.K. Sharma, C.Y. Ling, E. Birgersson, M. Vynnycky, M. Han, Verified reduction of dimensionality for an all-vanadium redox flow battery model, *J. Power Sources* 279 (2015) 345–350, <https://doi.org/10.1016/j.jpowsour.2015.01.019>.
- [17] G. Qiu, A.S. Joshi, C.R. Dennison, K.W. Knehr, E.C. Kumbur, Y. Sun, 3-D pore-scale resolved model for coupled species/charge/fluid transport in a vanadium redox flow battery, *Electrochim. Acta* 64 (2012) 46–64, <https://doi.org/10.1016/j.electacta.2011.12.065>.
- [18] X. Ma, H. Zhang, F. Xing, A three-dimensional model for negative half cell of the vanadium redox flow battery, *Electrochim. Acta* 58 (2011) 238–246, <https://doi.org/10.1016/j.electacta.2011.09.042>.
- [19] Q. Xu, T.S. Zhao, P.K. Leung, Numerical investigations of flow field designs for vanadium redox flow batteries, *Appl. Energy* 105 (2013) 47–56, <https://doi.org/10.1016/j.apenergy.2012.12.041>.
- [20] Q. Zheng, H. Zhang, F. Xing, X. Ma, X. Li, G. Ning, A three-dimensional model for thermal analysis in a vanadium flow battery, *Appl. Energy* 113 (2014) 1675–1685, <https://doi.org/10.1016/j.apenergy.2013.09.021>.
- [21] C. Yin, Y. Gao, S. Guo, H. Tang, A coupled three dimensional model of vanadium redox flow battery for flow field designs, *Energy* 74 (2014) 886–895, <https://doi.org/10.1016/j.energy.2014.07.066>.
- [22] K. Oh, H. Yoo, J. Ko, S. Won, H. Ju, Three-dimensional, transient, nonisothermal model of all-vanadium redox flow batteries, *Energy* 81 (2015) 3–14, <https://doi.org/10.1016/j.energy.2014.05.020>.
- [23] H. Al-Fetlawi, A.A. Shah, F.C. Walsh, Non-isothermal modelling of the all-vanadium redox flow battery, *Electrochim. Acta* 55 (2009) 78–89, <https://doi.org/10.1016/j.electacta.2009.08.009>.
- [24] D. You, H. Zhang, J. Chen, A simple model for the vanadium redox battery, *Electrochim. Acta* 54 (27) (2009) 6827–6836, <https://doi.org/10.1016/j.electacta.2009.06.086>.
- [25] A.A. Shah, H. Al-Fetlawi, F.C. Walsh, Dynamic modelling of hydrogen evolution effects in the all-vanadium redox flow battery, *Electrochim. Acta* 55 (3) (2010) 1125–1139, <https://doi.org/10.1016/j.electacta.2009.10.022>.
- [26] K.W. Knehr, E. Agar, C.R. Dennison, A.R. Kalidindi, E.C. Kumbur, A transient vanadium flow battery model incorporating vanadium crossover and water transport through the membrane, *J. Electrochem. Soc.* 159 (9) (2012) A1446–A1459, <https://doi.org/10.1149/2.017209jes>.
- [27] A.K. Sharma, M. Vynnycky, C.Y. Ling, E. Birgersson, M. Han, The quasi-steady state of all-vanadium redox flow batteries: a scale analysis, *Electrochim. Acta* 147 (2014) 657–662, <https://doi.org/10.1016/j.electacta.2014.09.134>.
- [28] M. Vynnycky, Analysis of a model for the operation of a vanadium redox battery, *Energy* 36 (2011) 2242–2256, <https://doi.org/10.1016/j.energy.2010.03.060>.
- [29] C.L. Chen, H.K. Yeoh, M.H. Chakrabarti, An enhancement to Vynnycky's model for the all-vanadium redox flow battery, *Electrochim. Acta* 120 (2014) 167–179, <https://doi.org/10.1016/j.electacta.2013.12.074>.
- [30] X. Ke, J.I.D. Alexander, J.M. Prahl, R.F. Savinell, Flow distribution and maximum current density studies in redox flow batteries with a single passage of the serpentine flow channel, *J. Power Sources* 270 (2014) 646–657, <https://doi.org/10.1016/j.jpowsour.2014.07.155>.
- [31] A.A. Shah, R. Tangirala, R. Singh, R.G.A. Wills, F.C. Walsh, A dynamic unit cell model for the all-vanadium flow battery, *J. Electrochem. Soc.* 158 (6) (2011) A671–A677, <https://doi.org/10.1149/1.3561426>.
- [32] S.K. Murthy, A.K. Sharma, C. Choo, E. Birgersson, Analysis of concentration overpotential in an all-vanadium redox flow battery, *J. Electrochem. Soc.* 165 (9) (2018) A1746–A1752, <https://doi.org/10.1149/2.0681809jes>.
- [33] D.E. Eapen, S.R. Choudhury, R. Rengaswamy, Low grade heat recovery for power generation through electrochemical route: vanadium redox flow battery, a case study, *Appl. Surf. Sci.* 474 (2019) 262–268, <https://doi.org/10.1016/j.apsusc.2018.02.025>.
- [34] J. Newman, K.E. Thomas-Alyea, *Electrochemical Systems*, third ed., Wiley-Interscience, New York, US, 2004.
- [35] X. Ke, J.M. Prahl, J.I.D. Alexander, J.S. Wainright, T.A. Zawodzinski, R.F. Savinell, Rechargeable redox flow batteries: flow fields, stacks and design considerations, *Chem. Soc. Rev.* 47 (2018) 8721–8743, <https://doi.org/10.1039/c8cs00072g>.
- [36] I. Mayrhuber, C.R. Dennison, V. Kalra, E.C. Kumbur, Laser-perforated carbon paper electrodes for improved mass-transport in high power density vanadium redox flow batteries, *J. Power Sources* 260 (2014) 251–258, <https://doi.org/10.1016/j.jpowsour.2014.03.007>.
- [37] Q. Zheng, F. Xing, X. Li, G. Ning, H. Zhang, Flow field design and optimization based on the mass transport polarization regulation in a flow-through type vanadium flow battery, *J. Power Sources* 324 (2016) 402–411, <https://doi.org/10.1016/j.jpowsour.2016.05.110>.
- [38] C. Yin, Y. Gao, G. Xie, T. Li, H. Tang, Three dimensional multi-physical modeling study of interdigitated flow field in porous electrode for vanadium redox flow battery, *J. Power Sources* 438 (2019) 227023, <https://doi.org/10.1016/j.jpowsour.2019.227023>.
- [39] H. Schlichting, *Boundary Layer Theory*, seventh ed., McGraw-Hill Publishing, New York, 1979.
- [40] A.J. Bard, L.R. Faulkner, *Electrochemical Methods, Fundamentals and Applications*, second ed., John Wiley & Sons, Ltd, New York, NY, USA, 2001.
- [41] A.F. Mills, *Basic Heat and Mass Transfer*, second ed., Prentice Hall, Upper Saddle River, NJ, 1999.
- [42] Z. Xu, A reduced-boundary-function method for convective heat transfer with axial heat conduction and viscous dissipation, *J. Heat Tran.* 134 (7) (2012), 071705, <https://doi.org/10.1115/1.4006112>.
- [43] V. Yu, D. Chen, Dynamic model of a vanadium redox flow battery for system performance control, *J. Sol. Energy Eng.* 136 (2) (2014) 021005, <https://doi.org/10.1115/1.4024928>.
- [44] Q. Xu, T.S. Zhao, Determination of the mass-transport properties of vanadium ions through the porous electrodes of vanadium redox flow batteries, *Phys. Chem. Chem. Phys.* 15 (26) (2013) 10841–10848, <https://doi.org/10.1039/c3cp51944a>.
- [45] G. Merei, S. Adler, D. Magnor, M. Leuthold, D.U. Sauer, Multi-physics model for a vanadium redox flow battery, *Energy Procedia* 46 (2014) 194–203, <https://doi.org/10.1016/j.egypro.2014.01.173>.
- [46] S. Kim, Vanadium redox flow batteries: electrochemical engineering. *Energy Storage Devices*, IntechOpen, 2019, pp. 1–19.
- [47] D.K. Kim, S.J. Yoon, J. Lee, S. Kim, Parametric study and flow rate optimization of all-vanadium redox flow batteries, *Appl. Energy* 228 (2018) 891–901, <https://doi.org/10.1016/j.apenergy.2018.06.094>.
- [48] R. David, L. David, *Handbook of Chemistry and Physics*, 84th Edition, CRC Press, Inc, Boca Raton, Florida, 2003.
- [49] T. Yamamura, N. Watanabe, T. Yano, Y. Shiokawa, Electron-transfer kinetics of $\text{Np}^{3+}/\text{Np}^{4+}$, $\text{NpO}_2^+/\text{NpO}_2^{2+}$, $\text{V}^{2+}/\text{V}^{3+}$, and $\text{VO}^{2+}/\text{VO}_2^+$ at carbon electrodes, *J. Electrochim. Soc.* 152 (4) (2005) A830–A836, <https://doi.org/10.1149/1.1870794>.